Journal of Scientific Computing (2019) 79:369–388
https://doi.org/10.1007/s10915-018-0856-x

Numerical Simulations of Viscoelastic Fluid Flows Past a Transverse Slot Using Least-Squares Finite Element Methods

Hsueh-Chen Lee[1] · **Hyesuk Lee**[2]

Received: 3 March 2018 / Revised: 12 August 2018 / Accepted: 12 October 2018 /
Published online: 26 October 2018

Abstract
This paper presents a least-squares (LS) finite element method for linear Phan-Thien–Tanner (PTT) viscoelastic fluid flows. We consider stabilized weights in the LS method for the viscoelastic model and prove that the LS approximation converges to the linearized solutions of the linear PTT model; the convergence is at the optimal rate for the velocity in the H^1-norm and at suboptimal rates for the stress and pressure in the L^2-norm, respectively. For numerical experiments we first consider the flow through a planar channel to illustrate our theoretical results. The LS method is then applied to a flow through the slot channel with two depth ratios and the effects of physical parameters are discussed. Numerical solutions of the channel problem indicate that flow characteristics of the viscoelastic polymer solution are described by the results obtained using the method. Furthermore, we present the hole pressure for various Weissenberg numbers, and compare with that derived from the Higashitani–Pritchard (HP) theory.

Keywords Least-squares · The PTT model · Hole pressure · Normal-stress difference · Transverse slot · Weissenberg number

1 Introduction

The objective of this study is to develop a least-squares finite element method (LS) for analyzing linear Phan-Thien–Tanner (PTT) viscoelastic fluid flow problems. In contrast to Newtonian model problems, PTT model problems are associated with fluid viscosity, elasticity, and memory. Phan-Thien and Tanner [19] developed a three-parameter model by using molecular concepts that are based on nonlinear stress. This model has gained prominencebecause it describes the power-law regions for viscosity and normal-stress coefficients.

✉ Hsueh-Chen Lee
87013@mail.wzu.edu.tw; hsuehchen.lee@gmail.com

Hyesuk Lee
hklee@clemson.edu

[1] General Education Center, Wenzao Ursuline University of Languages, Kaohsiung, Taiwan

[2] Department of Mathematical Sciences, Clemson University, Clemson, SC 29634-0975, USA

In the PTT model, the extra-stress is written as a superposition of the polymeric and viscous stresses, i.e.

$$\boldsymbol{\tau} = \boldsymbol{\tau}_p + \boldsymbol{\tau}_s.$$

The viscous stress, which is associated with a solvent in some applications, is Newtonian, i.e.,

$$\boldsymbol{\tau}_s = 2\eta_s \mathbf{D}(\mathbf{u}), \tag{1}$$

where η_s is a constant viscosity and $\mathbf{D}(\mathbf{u}) = 0.5(\nabla\mathbf{u} + \nabla\mathbf{u}^T)$ is the standard strain rate tensor with the velocity $\mathbf{u}$. In the linear PTT model, the polymer contribution to the stress obeys the following equation [1,17],

$$\boldsymbol{\tau}_p \left(1 + \frac{\epsilon\lambda}{\eta_p}(tr(\boldsymbol{\tau}_p))\right) + \lambda(\mathbf{u}\cdot\nabla\boldsymbol{\tau}_p - A(\nabla\mathbf{u}, \boldsymbol{\tau}_p)) = 2\eta_p\mathbf{D}(\mathbf{u}), \tag{2}$$

where

$$A(\nabla\mathbf{u}, \boldsymbol{\tau}_p) = (\nabla\mathbf{u})^T\cdot\boldsymbol{\tau}_p + \boldsymbol{\tau}_p\cdot\nabla\mathbf{u}.$$

In (2), λ is a relaxation time and η_p is the polymeric contribution to the viscosity. The extensibility parameter ϵ lies in the range $0 \le \epsilon \le 1$, and setting $\epsilon = 0$ reduces the model to the Oldroyd-B model. Replacing the first term of (2) by $\boldsymbol{\tau}_p\, exp(\frac{\epsilon\lambda}{\eta_p}(tr(\boldsymbol{\tau}_p)))$ yields the exponential form, which is another extensively used PTT model [1,2].

Consider the steady-state, incompressible Navier–Stokes problem in a two-dimensional bounded domain Ω with the Lipschitz continuous boundary Γ. Collecting (2), we have the linear PTT model written as

$$\begin{aligned}
\rho(\mathbf{u}\cdot\nabla\mathbf{u}) - \nabla\cdot\boldsymbol{\tau}_p - \nabla\cdot\boldsymbol{\tau}_s + \nabla p &= \mathbf{f} \ \text{ in } \Omega,\\
\nabla\cdot\mathbf{u} &= 0 \ \text{ in } \Omega,\\
\boldsymbol{\tau}_s - 2\eta_s\mathbf{D}(\mathbf{u}) &= \mathbf{0} \ \text{ in } \Omega,\\
\boldsymbol{\tau}_p + \lambda(\mathbf{u}\cdot\nabla\boldsymbol{\tau}_p - A(\nabla\mathbf{u}, \boldsymbol{\tau}_p)) + \frac{\epsilon\lambda tr(\boldsymbol{\tau}_p)\boldsymbol{\tau}_p}{\eta_p} - 2\eta_p\mathbf{D}(\mathbf{u}) &= \mathbf{0} \ \text{ in } \Omega,\\
\mathbf{u} &= \mathbf{0} \ \text{ on } \Gamma,
\end{aligned} \tag{3}$$

where ρ is the density and $\mathbf{f}$ is the body force vector. We assume that the scalar pressure p satisfies a zero mean constraint to ensure the uniqueness of pressure.

As pointed out in [1], this first-order problem can be nondimensionalized as:

$$Re(\mathbf{u}\cdot\nabla\mathbf{u}) - \nabla\cdot\boldsymbol{\tau}_p - \nabla\cdot\boldsymbol{\tau}_s + \nabla p = \mathbf{f} \ \text{ in } \Omega, \tag{4}$$

$$\nabla\cdot\mathbf{u} = 0 \ \text{ in } \Omega, \tag{5}$$

$$\boldsymbol{\tau}_s - 2\beta\mathbf{D}(\mathbf{u}) = \mathbf{0} \ \text{ in } \Omega, \tag{6}$$

$$\boldsymbol{\tau}_p + We(\mathbf{u}\cdot\nabla\boldsymbol{\tau}_p - A(\nabla\mathbf{u}, \boldsymbol{\tau}_p)) + \frac{\epsilon We tr(\boldsymbol{\tau}_p)\boldsymbol{\tau}_p}{(1-\beta)} - 2(1-\beta)\mathbf{D}(\mathbf{u}) = \mathbf{0} \ \text{ in } \Omega, \tag{7}$$

$$\mathbf{u} = \mathbf{0} \ \text{ on } \Gamma, \tag{8}$$

where Re is the Reynolds number, $Re \equiv L_c U_c \rho/\eta_0$, in which $\eta_o = \eta_s + \eta_p$ is the zero-shear-rate viscosity, L_c and U_c are characteristic length and velocity, respectively. $\beta \equiv \eta_s/\eta_o \in [0, 1]$ is the ratio of solvent viscosity to the total zero-shear-rate viscosity and $We \ge 0$ is the Weissenberg number defined by $We \equiv \lambda U_c/L_c$. In the case of $We = 0$, the model reduces to a Newtonian model, the Navier–Stokes equations.

Various developments have been reported in the use of LS methods for viscoelastic flow problems [4,6,7,11,22]. LS methods use the L^2-norm of the residuals of the continuity equation multiplied by appropriately adjusted weights. These problems can be conveniently simulated by splitting the extra-stress tensor into viscous and elastic components by changing the variables in the LS formulations. LS methods offer several theoretical and computational advantages [3]. Discretization generates an algebraic system that is always symmetric and positive definite, and a single approximating space for all variables can be used for programming LS methods [6]. The LS functional also provides a local and inexpensive a posteriori error estimate that is highly effective and reliable for error control [16]. In [8], Coronado et al. presented a Galerkin least-squares (GLS) method for the Oldroyd-B model, where LS stabilization terms are added to the standard Galerkin formulation. In their work, appropriately chosen weights are used in the LS stabilization terms and equal order linear interpolation functions are considered for numerical experiments. In our previous research [6,7,11], nonlinear functions have been used for LS methods (NWLS) to solve viscoelastic fluid flows past a 4-to-1 contraction. The results show that the NWLS solutions can be improved by sufficiently weighting the mass equation and by the choice of nonlinear weights on velocity gradient and constitutive equations; however, the numerical computations have been performed at low We numbers without the inertial term.

On the basis of these studies, we present a linear weighted LS method for analyzing the linear PTT viscoelastic fluid flows past a transverse slot. Numerical simulations of high Weissenberg flows are known to be challenging due to some mathematical and physical issues [17]. In this study we consider an LS method involving appropriate weights to prevent the violation of mass conservation and to improve convergence of numerical schemes for the high Weissenberg flows [6,11]. We use a residual-type a posteriori error estimator for the LS functional to adjust the weight of the mass equation [15], and use a weight function of the extensibility parameter and the Weissenberg number. For viscoelastic fluid flows, the use of the LS method with constant weights is much simpler than the NWLS method [6,11] or the GLS method [8]. Furthermore, we estimate the coercivity and continuity for the homogeneous LS functional, which involves the sum of equation residuals measured in L^2-norm. A similar proof is given in [22] for a non-weighted LS functional, but we present our detailed proof involving the convection term for the completeness of this paper. Even though we provide the analysis of error bounds with the condition of a small solution or small Weissenberg number, our numerical results in Sect. 4 show this assumption may not be necessary for simulations.

One of numerical examples considered in this study is the viscoelastic fluid flow between two parallel plates past a transverse slot (Fig. 1). Pressure transducers mounted at points a and b show the readings of $P_a = (p_a - \boldsymbol{\tau}^a_{pyy})$ and $P_b = (p_b - \boldsymbol{\tau}^b_{pyy})$, respectively. $P_h = P_b - P_a = (p_b - p_a) + (\boldsymbol{\tau}^a_{pyy} - \boldsymbol{\tau}^b_{pyy})$ represents the hole pressure (P_h), with $P_h > 0$ for polymeric fluids and $P_h = 0$ for the Newtonian flow. These are the feature of viscoelastic effects [20]. Numerous studies have been attempted to improve understanding of such a flow. In [18], Tanner and Pipkin presented theoretical and experimental results for the creeping flow of a second-order fluid over a slot. They indicated that the hole pressure was one-quarter of the first normal-stress difference (N_1). Higashitani and Pritchard [9] used a different approach and developed the Higashitani–Pritchard (HP) equation to estimate the hole pressure (P_h):

$$P_h = \int_0^{\boldsymbol{\tau}^b_w} \frac{N_1}{2\boldsymbol{\tau}} d\boldsymbol{\tau}, \tag{9}$$

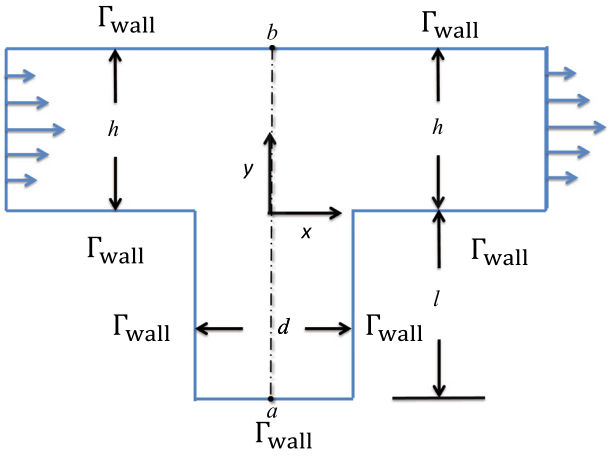

Fig. 1 The slot channel

where N_1 is the primary normal-stress difference in terms of the shear stress in a simple shear flow, and $\boldsymbol{\tau}_w^b$ is the disturbed wall shear stress at point b shown in Fig. 1. Note that the HP equation (9), is formulated in [20] under the symmetric assumption of the streamlines, shear stress, and axial stress about the centreline of the slot. In [20], the results show that this equation is valid only for a creeping flow with a low We. The streamlines of pressure with different values of d/h and l/h are shown in [10]. They indicated that as the slot become deeper, it is expected that the shear rate at the bottom would diminish and the flow pattern would change at the bottom of the slot.

We apply our LS method to simulate flows through the transverse slot considered in [21] and address the physical parameter effects. The resulting hole pressure is evaluated numerically for various We, and compared with that derived form the HP theory. Numerical results show that (9) is valid when We is low, as demonstrated in [20] and invalid when We is high. In other numerical example of a planar channel problem, we demonstrate that numerical solutions exhibit the highest convergence rates, which are consistent with the theoretically predicted rates, when conforming piecewise polynomial elements are used for all variables.

The rest of this paper is organized as follows. Section 2 presents the notation, preliminaries, and coercivity and continuity estimates for the LS functional. Section 3 presents error estimates of the LS approximations. Section 4 presents numerical results for flows through a planar channel and past a slot in a channel, respectively. Finally, Sect. 5 offers concluding remarks.

2 An LS Finite Element Functional

Let $\mathcal{D}(\Omega)$ be the linear space of infinitely differentiable functions with compact supports on Ω, that is,

$$\mathcal{D}\left(\bar{\Omega}\right) = \{\psi|_{\Omega} : \psi \in \mathcal{D}(\mathcal{O}) \text{ for some open subsect } \subset \mathcal{O} \subset \mathbb{R}^2\},$$

where $\bar{\Omega}$ is the closure of Ω [13]. Let $H^s(\Omega)$, $s \geq 0$, be the Sobolev spaces with the standard associated inner products $(\cdot,\cdot)_s$ and their respective norms $\|\cdot\|_s$. For $s = 0$, $H^s(\Omega)$ coincides with $L^2(\Omega)$, and $H_0^s(\Omega)$ denotes the closure of $\mathcal{D}(\Omega)$ with respect to the norm $\|\cdot\|_s$. For

positive values of s, the space $H^{-s}(\Omega)$ is defined as the dual space of $H_0^s(\Omega)$ equipped with the norm

$$\|\sigma\|_{-s} := \sup_{0\neq v\in H_0^s(\Omega)} \frac{\langle \sigma, v\rangle}{\|v\|_s},$$

where $(\cdot,\cdot)$ is the duality pairing between $H^{-s}(\Omega)$ and $H_0^s(\Omega)$ when there is no risk of confusion.

The function spaces used in our variational formulations are defined as

$$\boldsymbol{V} := (H_0^1(\Omega))^2, \quad Q := L_0^2(\Omega)\cap H^1(\Omega),$$
$$\boldsymbol{\Sigma}_s := \{\boldsymbol{\sigma} \mid \boldsymbol{\sigma}\in (H^1(\Omega))^{2\times 2},\ \sigma_{ij}=\sigma_{ji}\}, \quad \boldsymbol{\Sigma}_p := \boldsymbol{\Sigma}_s$$

and let the product space $\boldsymbol{\Phi} := \boldsymbol{V}\times Q\times \boldsymbol{\Sigma}_s\times \boldsymbol{\Sigma}_p$.

Based on [4], linearizing (4)–(8) about the approximation

$$\mathbf{u}\cdot\nabla\mathbf{u} \approx \mathbf{u}_1\cdot\nabla\mathbf{u} + \mathbf{u}\cdot\nabla\mathbf{u}_1 - \mathbf{u}_1\cdot\nabla\mathbf{u}_1,$$
$$\boldsymbol{\tau}_{p1} \approx \boldsymbol{\tau}_p,\ \mathbf{u}_1\approx\mathbf{u},$$

where we assume $\nabla\cdot\mathbf{u}_1 = 0$ and

$$\max\{\|\mathbf{u}_1\|_\infty,\ \|\nabla\mathbf{u}_1\|_\infty, \|\boldsymbol{\tau}_{p1}\|_\infty,\ \|\nabla\boldsymbol{\tau}_{p1}\|_\infty\} \le M < \infty, \tag{10}$$

results in the following replacement rules:

$$\mathbf{u}\cdot\nabla\boldsymbol{\tau_p} \approx \mathbf{u}_1\cdot\nabla\boldsymbol{\tau_p} + \mathbf{u}\cdot\nabla\boldsymbol{\tau_{p_1}} - \mathbf{u}_1\cdot\nabla\boldsymbol{\tau_{p_1}},$$
$$A(\nabla\mathbf{u},\boldsymbol{\tau}_p) \approx A(\nabla\mathbf{u}_1,\boldsymbol{\tau_p}) + A(\nabla\mathbf{u},\boldsymbol{\tau}_{p1}) - A(\nabla\mathbf{u}_1,\boldsymbol{\tau}_{p1}),$$
$$tr(\boldsymbol{\tau}_p)\boldsymbol{\tau}_p \approx tr(\boldsymbol{\tau}_{p1})\boldsymbol{\tau}_p + tr(\boldsymbol{\tau}_p)\boldsymbol{\tau}_{p1} - tr(\boldsymbol{\tau}_{p1})\boldsymbol{\tau}_{p1}.$$

Note that $\mathbf{u}_1$ and $\boldsymbol{\tau}_{p1}$ will be replaced by $\mathbf{u}_\ell^h$ and $\boldsymbol{\tau}_{p\ell}^h$ which are the ℓth iterative approximations in Sect. 3.

The linearized system of the linear PTT model may now be written as

$$Re(\mathbf{u}_1\cdot\nabla\mathbf{u} + \mathbf{u}\cdot\nabla\mathbf{u}_1) - \nabla\cdot\boldsymbol{\tau}_p - \nabla\cdot\boldsymbol{\tau}_s + \nabla p = \mathbf{f_1} \text{ in } \Omega, \tag{11}$$
$$\nabla\cdot\mathbf{u} = 0 \text{ in } \Omega, \tag{12}$$
$$\boldsymbol{\tau}_s - 2\beta\mathbf{D}(\mathbf{u}) = \mathbf{0} \text{ in } \Omega, \tag{13}$$
$$\boldsymbol{\tau}_p + We\left(\mathbf{u}_1\cdot\nabla\boldsymbol{\tau_p}\right) + B(\mathbf{u},\boldsymbol{\tau_p}) + C(\boldsymbol{\tau_p}) - 2(1-\beta)\mathbf{D}(\mathbf{u}) = \mathbf{f_2} \text{ in } \Omega, \tag{14}$$
$$\mathbf{u} = \mathbf{0} \text{ on } \Gamma, \tag{15}$$

where we define

$$\mathbf{f_1} = Re(\mathbf{u}_1\cdot\nabla\mathbf{u}_1) + \mathbf{f},$$
$$B(\mathbf{u},\boldsymbol{\tau_p}) = We\left(\mathbf{u}\cdot\nabla\boldsymbol{\tau}_{p_1} - A(\nabla\mathbf{u}_1,\boldsymbol{\tau}_p) - A(\nabla\mathbf{u},\boldsymbol{\tau}_{p1})\right),$$
$$C(\boldsymbol{\tau_p}) = (\epsilon We/(1-\beta))\left(tr(\boldsymbol{\tau}_{p1})\boldsymbol{\tau}_p + tr(\boldsymbol{\tau}_p)\boldsymbol{\tau}_{p1}\right),$$
$$\mathbf{f_2} = We\left(\mathbf{u}_1\cdot\nabla\boldsymbol{\tau}_{p_1} - A(\nabla\mathbf{u}_1,\boldsymbol{\tau}_{p_1})\right) + (\epsilon We/(1-\beta))(tr(\boldsymbol{\tau}_{p1})\boldsymbol{\tau}_{p1}).$$

The LS functional for (11)–(15) is given by

$$\begin{aligned} &J(\mathbf{u},p,\boldsymbol{\tau}_s,\boldsymbol{\tau}_p;\mathbf{F})\\ &= \left\|Re(\mathbf{u}_1\cdot\nabla\mathbf{u} + \mathbf{u}\cdot\nabla\mathbf{u}_1) - \nabla\cdot\boldsymbol{\tau}_s - \nabla\cdot\boldsymbol{\tau}_p + \nabla p - \mathbf{f_1}\right\|_0^2\\ &\quad + K\|\nabla\cdot\mathbf{u}\|_0^2 + \|\boldsymbol{\tau}_s - 2\beta\mathbf{D}(\mathbf{u})\|_0^2\\ &\quad + W\left\|\boldsymbol{\tau}_p + We\left(\mathbf{u}_1\cdot\nabla\boldsymbol{\tau}_p\right) + B(\mathbf{u},\boldsymbol{\tau_p}) + C(\boldsymbol{\tau_p}) - 2(1-\beta)\mathbf{D}(\mathbf{u}) - \mathbf{f_2}\right\|_0^2, \end{aligned} \tag{16}$$

where the positive constant K is a weight of the mass equation. The mass conservation weight is chosen as $K = 10^m$ for $0 \le m \le 10$ based on [6,11–13,15]. Their results indicate that LS solutions can be improved by sufficiently weighting the divergence term. In addition, the weight W is introduced to stabilize the LS form at a high We and ϵ in the constitutive equation. The weight given by $W = (1 + We + \epsilon)^2$ will be used, which is simpler than the nonlinear weight of the NWLS method in [6,11]. In [6,11], some physical parameters are used in a nonlinear weighting function for reflecting flow characteristics of the viscoelastic polymer solution. The nonlinear weighting function stabilizes the least-squares form in the constitutive equation and improves convergence rates over the case of no weighting. In [8,11], appropriately designed weight functions about We are employed when using the NWLS and GLS methods to solve the Oldroyd-B model at high We numbers. In this work we use the simpler weight $W = (1 + We + \epsilon)^2$ based on successful numerical tests of those methods and our preliminary test.

We now consider the LS minimization problem for the solution of system (11)−(15) defined as: choose $\boldsymbol{U} \in \boldsymbol{\Phi}$ such that

$$J(\boldsymbol{U}; \mathbf{F}) = \inf_{\boldsymbol{V} \in \boldsymbol{\Phi}} J(\boldsymbol{V}; \mathbf{F}), \tag{17}$$

where $\boldsymbol{U} = (\mathbf{u}, p, \boldsymbol{\tau}_s, \boldsymbol{\tau}_p)$ and $\boldsymbol{V} = (\mathbf{v}, q, \boldsymbol{\sigma}_s, \boldsymbol{\sigma}_p)$.

To appropriately adjust the weight value K in numerical experiments, we will also consider the LS functional of the residual of the system (4)–(8), as follows:

$$\begin{aligned} & g(\boldsymbol{U}; \mathbf{f}) \\ &= \left\| Re(\mathbf{u} \cdot \nabla \mathbf{u}) - \nabla \cdot \boldsymbol{\tau}_s - \nabla \cdot \boldsymbol{\tau}_p + \nabla p - \mathbf{f} \right\|_0^2 + \| \nabla \cdot \mathbf{u} \|_0^2 + \| \boldsymbol{\tau}_s - 2\beta \mathbf{D}(\mathbf{u}) \|_0^2 \\ &\quad + \left\| \boldsymbol{\tau}_p + We(\mathbf{u} \cdot \nabla \boldsymbol{\tau}_p - A(\nabla \mathbf{u}, \boldsymbol{\tau}_p)) + \frac{\epsilon We}{(1-\beta)} tr(\boldsymbol{\tau}_p) \boldsymbol{\tau}_p - 2(1-\beta)\mathbf{D}(\mathbf{u}) \right\|_0^2 \end{aligned} \tag{18}$$

$\forall\, \boldsymbol{U} = (\mathbf{u}, \mathbf{p}, \boldsymbol{\tau}_s, \boldsymbol{\tau}_p) \in \boldsymbol{\Phi}$. The L^2 functional $g(\boldsymbol{U}; \mathbf{f})$ is an a posteriori error estimate for the first-order system LS method as in [12,15] and serves as an indicator to adjust the weight $K = 10^m$.

Denote two norms on $\boldsymbol{\Phi}$ as

$$|||\boldsymbol{U}||| = \left(\|\mathbf{u}\|_1^2 + \|p\|_0^2 + \|\boldsymbol{\tau}_s\|_0^2 + \|\boldsymbol{\tau}_p\|_0^2 \right)^{1/2} \tag{19}$$

and

$$|||\boldsymbol{U}|||_1 = \left(Re^2 \|\mathbf{u}\|_1^2 + \|p\|_1^2 + \|\boldsymbol{\tau}_s\|_1^2 + \|\boldsymbol{\tau}_p\|_1^2 \right)^{1/2} \tag{20}$$

$\forall \boldsymbol{U} = (\mathbf{u}, p, \boldsymbol{\tau}_s, \boldsymbol{\tau}_p) \in \boldsymbol{\Phi}$. We now derive some a priori estimates for the first-order system (16), i.e., the coercivity and continuity estimates for the homogeneous LS functional. As mentioned in Sect. 1, a similar proof is found in [22], however we present a detailed proof because the a priori estimates will play crucial roles in the error estimation of our weighted LS method.

Theorem 1 *For any $\boldsymbol{U} = (\mathbf{u}, p, \boldsymbol{\tau}_s, \boldsymbol{\tau}_p) \in \boldsymbol{\Phi}$, there are positive constants, c_0 and c_1, which depend on Ω, β, We, ϵ, and M in (10), such that*

$$c_0 \, |||\boldsymbol{U}|||^2 \le J(\boldsymbol{U}; \mathbf{0}) \le c_1 \, |||\boldsymbol{U}|||_1^2 , \tag{21}$$

for sufficiently small M in Ω.

Proof The upper bound follows naturally from the triangle inequality. We proceed to show the validity of the lower bound in (21). For the lower bound, we define

$$H := \left\|-\nabla\cdot\boldsymbol{\tau}_s - \nabla\cdot\boldsymbol{\tau}_p + \nabla p\right\|_0^2 + \|\nabla\cdot\mathbf{u}\|_0^2 + \|\boldsymbol{\tau}_s - 2\beta\mathbf{D}(\mathbf{u})\|_0^2 + \left\|\boldsymbol{\tau}_p + W_e\left(\mathbf{u}_1\cdot\nabla\boldsymbol{\tau}_{\mathrm{p}}\right) - 2(1-\beta)\boldsymbol{D}(\mathbf{u})\right\|_0^2,$$

as shown in [11]. By Green's formula and the Cauchy–Schwarz inequality, for any $\boldsymbol{\varphi} \in (H_0^1(\Omega))^2$,

$$\begin{aligned}\langle\nabla p, \boldsymbol{\varphi}\rangle &= \left\langle-\nabla\cdot\boldsymbol{\tau}_s - \nabla\cdot\boldsymbol{\tau}_p + \nabla p, \boldsymbol{\varphi}\right\rangle + \langle\boldsymbol{\tau}_s, \boldsymbol{D}(\boldsymbol{\varphi})\rangle + \left\langle\boldsymbol{\tau}_p, \boldsymbol{D}(\boldsymbol{\varphi})\right\rangle &(22)\\ &\le \left(\left\|-\nabla\cdot\boldsymbol{\tau}_s - \nabla\cdot\boldsymbol{\tau}_p + \nabla p\right\|_0 + \|\boldsymbol{\tau}_s\|_0 + \left\|\boldsymbol{\tau}_p\right\|_0\right)\|\varphi\|_1 . &(23)\end{aligned}$$

Using the inequality (see [5])

$$\|p\|_0 \le C_1\|\nabla p\|_{-1},$$

we have

$$\|p\|_0 \le C_1\|\nabla p\|_{-1} \le C_1\left(\left\|-\nabla\cdot\boldsymbol{\tau}_s - \nabla\cdot\boldsymbol{\tau}_p + \nabla p\right\|_0 + \|\boldsymbol{\tau}_s\|_0 + \left\|\boldsymbol{\tau}_p\right\|_0\right).$$

Hence, we have the estimate

$$\|p\|_0 \le C_1\left(\mathrm{H}^{1/2} + \left\|\boldsymbol{\tau}_p\right\|_0 + \|\boldsymbol{\tau}_s\|_0\right). \tag{24}$$

Note that $\left\langle\mathbf{u}_1\cdot\nabla\boldsymbol{\tau}_p, \boldsymbol{\tau}_p\right\rangle = 0$ with $\nabla\cdot\mathbf{u}_1 = 0$ and $\mathbf{u_1}|_\Gamma = 0$, therefore we also have

$$\frac{2\beta}{1-\beta}\left\|\boldsymbol{\tau}_p\right\|_0^2 = \left\langle\boldsymbol{\tau}_p + We(\mathbf{u_1}\cdot\nabla\boldsymbol{\tau}_p) - 2(1-\beta)\boldsymbol{D}(\mathbf{u}), \frac{2\beta}{1-\beta}\boldsymbol{\tau}_p\right\rangle + 4\beta\left\langle\boldsymbol{D}(\mathbf{u}), \boldsymbol{\tau}_p\right\rangle. \tag{25}$$

By Green's formula and the Poincaré–Friedrichs inequality

$$\|\mathbf{u}\|_0 \le C_2\|\boldsymbol{D}(\mathbf{u})\|_0, \tag{26}$$

we have

$$\begin{aligned}\left\langle\boldsymbol{\tau}_s + \boldsymbol{\tau}_p, \boldsymbol{D}(\mathbf{u})\right\rangle &= \left\langle-\nabla\cdot\boldsymbol{\tau}_s - \nabla\cdot\boldsymbol{\tau}_p + \nabla p, \mathbf{u}\right\rangle + \langle p, \nabla\cdot\mathbf{u}\rangle\\ &\le \|-\nabla\cdot\boldsymbol{\tau}_s - \nabla\cdot\boldsymbol{\tau}_p + \nabla p\|_0\|\mathbf{u}\|_0 + \|p\|_0\|\nabla\cdot\mathbf{u}\|_0\\ &\le H^{1/2}\|\mathbf{u}\|_0 + H^{1/2}\|p\|_0 \le H^{1/2}(C_2\|\boldsymbol{D}(\mathbf{u})\|_0 + \|p\|_0). &(27)\end{aligned}$$

Combining (26) and (27), we bound the linear combination

$$
\begin{aligned}
&4\beta^2\|\boldsymbol{D}(\mathbf{u})\|_0^2+\|\boldsymbol{\tau}_s\|_0^2+\frac{2\beta}{1-\beta}\|\boldsymbol{\tau}_p\|_0^2\\
&=\langle-\boldsymbol{\tau}_s+2\beta\boldsymbol{D}(\mathbf{u}),2\beta\boldsymbol{D}(\mathbf{u})\rangle+2\beta\langle\boldsymbol{\tau}_s,\boldsymbol{D}(\mathbf{u})\rangle+\langle\boldsymbol{\tau}_s-2\beta\boldsymbol{D}(\mathbf{u}),\boldsymbol{\tau}_s\rangle+2\beta\langle\boldsymbol{D}(\mathbf{u}),\boldsymbol{\tau}_s\rangle\\
&\quad+\left\langle\boldsymbol{\tau}_p+We(\mathbf{u}_1\cdot\nabla\boldsymbol{\tau}_p)-2(1-\beta)\boldsymbol{D}(\mathbf{u}),\frac{2\beta}{1-\beta}\boldsymbol{\tau}_p\right\rangle+4\beta\langle\boldsymbol{D}(\mathbf{u}),\boldsymbol{\tau}_p\rangle\\
&\le\|\boldsymbol{\tau}_s-2\beta\boldsymbol{D}(\mathbf{u})\|_0(2\beta)\|\boldsymbol{D}(\mathbf{u})\|_0+\|\boldsymbol{\tau}_s-2\beta\boldsymbol{D}(\mathbf{u})\|_0\|\boldsymbol{\tau}_s\|_0\\
&\quad+\|\boldsymbol{\tau}_p+We(\mathbf{u}_1\cdot\nabla\boldsymbol{\tau}_p)-2(1-\beta)\boldsymbol{D}(\mathbf{u})\|_0\left(\frac{2\beta}{1-\beta}\right)\|\boldsymbol{\tau}_p\|_0+\langle4\beta\boldsymbol{\tau}_s+4\beta\boldsymbol{\tau}_p,\boldsymbol{D}(\mathbf{u})\rangle\\
&\le\|\boldsymbol{\tau}_s-2\beta\boldsymbol{D}(\mathbf{u})\|_0(2\beta\|\boldsymbol{D}(\mathbf{u})\|_0+\|\boldsymbol{\tau}_s\|_0)\\
&\quad+\frac{2\beta}{1-\beta}\|\boldsymbol{\tau}_p+We(\mathbf{u}_1\cdot\nabla\boldsymbol{\tau}_p)-2(1-\beta)\boldsymbol{D}(\mathbf{u})\|_0\|\boldsymbol{\tau}_p\|_0+4\beta H^{1/2}(C_2\|\boldsymbol{D}(\mathbf{u})\|_0+\|p\|_0)\\
&\le\left[\|\boldsymbol{\tau}_s-2\beta\boldsymbol{D}(\mathbf{u})\|_0+\|\boldsymbol{\tau}_p+We(\mathbf{u}_1\cdot\nabla\boldsymbol{\tau}_p)-2(1-\beta)\boldsymbol{D}(\mathbf{u})\|_0\right]\\
&\quad\cdot\left(2\beta\|\boldsymbol{D}(\mathbf{u})\|_0+\|\boldsymbol{\tau}_s\|_0+\frac{2\beta}{1-\beta}\|\boldsymbol{\tau}_p\|_0\right)+4\beta H^{1/2}(C_2\|\boldsymbol{D}(\mathbf{u})\|_0+\|p\|_0)\\
&\le\sqrt{2}H^{1/2}\left(2\beta\|\boldsymbol{D}(\mathbf{u})\|_0+\|\boldsymbol{\tau}_s\|_0+\frac{2\beta}{1-\beta}\|\boldsymbol{\tau}_p\|_0\right)+4\beta H^{1/2}(C_2\|\boldsymbol{D}(\mathbf{u})\|_0+\|p\|_0)\\
&\le C(\beta)H^{1/2}(\|\boldsymbol{D}(\mathbf{u})\|_0+\|\boldsymbol{\tau}_s\|_0+\|\boldsymbol{\tau}_p\|_0+\|p\|_0),
\end{aligned}
\tag{28}
$$

where $C(\beta)$ is a constant depends on β. Using (24), (28) and Young's inequality,

$$
\begin{aligned}
\|\boldsymbol{D}(\mathbf{u})\|_0^2+\|\boldsymbol{\tau}_s\|_0^2+\|\boldsymbol{\tau}_p\|_0^2&\le C(\beta)H^{1/2}(\|\boldsymbol{D}(\mathbf{u})\|_0+\|\boldsymbol{\tau}_s\|_0+\|\boldsymbol{\tau}_p\|_0+H^{1/2})\\
&\le C(\beta)\left[\delta^{-1}H+3\delta(\|\boldsymbol{D}(\mathbf{u})\|_0^2+\|\boldsymbol{\tau}_s\|_0^2+\|\boldsymbol{\tau}_p\|_0^2)+H\right]
\end{aligned}
$$

for any $\delta>0$. By choosing sufficiently small δ, we establish

$$
\|\boldsymbol{D}(\mathbf{u})\|_0^2+\|\boldsymbol{\tau}_s\|_0^2+\|\boldsymbol{\tau}_p\|_0^2\le C(\beta)H. \tag{29}
$$

Using (24), (26), and (29), we obtain

$$
\||\boldsymbol{U}|\|^2\le C(\beta)H. \tag{30}
$$

To estimate a lower bound of $J(\boldsymbol{U};\mathbf{0})$ we first consider the following.

$$
\begin{aligned}
\|B(\mathbf{u},\boldsymbol{\tau_p})\|_0&=We\|\mathbf{u}\cdot\nabla\boldsymbol{\tau}_{p_1}-A(\nabla\mathbf{u}_1,\boldsymbol{\tau}_p)-A(\nabla\mathbf{u},\boldsymbol{\tau}_{p_1})\|_0\\
&\le We(M\|\mathbf{u}\|_0+2M\|\boldsymbol{\tau}_p\|_0+2M\|\nabla\mathbf{u}\|_0)\\
&\le 2We\,M(\sqrt{2}\|\mathbf{u}\|_1+\|\boldsymbol{\tau}_p\|_0), &(31)\\
\|C(\boldsymbol{\tau_p})\|_0&=(\epsilon We/(1-\beta))\|tr(\boldsymbol{\tau}_{p_1})\boldsymbol{\tau}_p+tr(\boldsymbol{\tau}_p)\boldsymbol{\tau}_{p1}\|_0\\
&\le(\epsilon We/(1-\beta))2M\|\boldsymbol{\tau}_p\|_0, &(32)\\
\|Re(\mathbf{u}_1\cdot\nabla\mathbf{u}+\mathbf{u}\cdot\nabla\mathbf{u}_1)\|_0&\le Re\,M(\|\nabla\mathbf{u}\|_0+\|\mathbf{u}\|_0)\\
&\le\sqrt{2}Re\,M\|\mathbf{u}\|_1. &(33)
\end{aligned}
$$

The estimates (31), (32) and the triangular inequality yield

$$
\begin{aligned}
\|B(\mathbf{u},\boldsymbol{\tau_p})+C(\boldsymbol{\tau_p})\|_0^2&\le\left[2MWe\left((1+\frac{\epsilon}{1-\beta})\|\boldsymbol{\tau}_p\|_0+\sqrt{2}\|\mathbf{u}\|_1\right)\right]^2\\
&\le We^2M^2\left[8(1+\frac{\epsilon}{1-\beta})^2\|\boldsymbol{\tau}_p\|_0^2+16\|\mathbf{u}\|_1^2\right].
\end{aligned}
\tag{34}
$$

By the way to choose the LS weights K, W, it is clear that $min\{\frac{1}{2}, K, \frac{W}{2}\} = \frac{1}{2}$. Hence, using the inequality $\|a+b\|^2 \geq \frac{1}{2}\|a\|^2 - \|b\|^2$ and the estimates (30), (33), (34), we have

$$
\begin{aligned}
&J(\boldsymbol{U};\mathbf{0}) \\
&\geq \frac{1}{2}\left\|-\nabla\cdot\boldsymbol{\tau}_s - \nabla\cdot\boldsymbol{\tau}_p + \nabla p\right\|_0^2 - \|Re(\mathbf{u}_1\cdot\nabla\mathbf{u} + \mathbf{u}\cdot\nabla\mathbf{u}_1)\|_0^2 \\
&\quad + K\|\nabla\cdot\mathbf{u}\|_0^2 + \|\boldsymbol{\tau}_s - 2\beta\mathbf{D}(\mathbf{u})\|_0^2 \\
&\quad + \frac{W}{2}\left\|\boldsymbol{\tau}_p + We\left(\mathbf{u}_1\cdot\nabla\boldsymbol{\tau}_p\right) - 2(1-\beta)\mathbf{D}(\mathbf{u})\right\|_0^2 - W\left\|B(\mathbf{u},\boldsymbol{\tau_p}) + C(\boldsymbol{\tau_p})\right\|_0^2 \\
&\geq \frac{1}{2}\Big(\left\|-\nabla\cdot\boldsymbol{\tau}_s - \nabla\cdot\boldsymbol{\tau}_p + \nabla p\right\|_0^2 + \|\nabla\cdot\mathbf{u}\|_0^2 + \|\boldsymbol{\tau}_s - 2\beta\mathbf{D}(\mathbf{u})\|_0^2 \\
&\quad + \left\|\boldsymbol{\tau}_p + We\left(\mathbf{u}_1\cdot\nabla\boldsymbol{\tau}_p\right) - 2(1-\beta)\mathbf{D}(\mathbf{u})\right\|_0^2\Big) \\
&\quad - \|Re(\mathbf{u}_1\cdot\nabla\mathbf{u} + \mathbf{u}\cdot\nabla\mathbf{u}_1)\|_0^2 - W\left\|B(\mathbf{u},\boldsymbol{\tau_p}) + C(\boldsymbol{\tau_p})\right\|_0^2 \\
&\geq \frac{1}{2}H - 2Re^2M^2\|\mathbf{u}\|_1^2 - We^2M^2W\left[8(1+\frac{\epsilon}{1-\beta})^2\|\boldsymbol{\tau}_p\|^2 + 16\|\mathbf{u}\|_1^2\right] \\
&\geq \frac{1}{2}H - M^2\left[(2Re^2 + 16We^2W)\|\mathbf{u}\|_1^2 + 8We^2W(1+\frac{\epsilon}{1-\beta})^2\|\boldsymbol{\tau}_p\|^2\right] \\
&\geq \frac{1}{2}C(\beta)\,|||\boldsymbol{U}|||^2 - M^2 max\left\{2Re^2 + 16We^2W,\ 8We^2W(1+\frac{\epsilon}{1-\beta})^2\right\}|||\boldsymbol{U}|||^2 .
\end{aligned}
$$

Therefore, if M is sufficiently small

$$J(\boldsymbol{U};\mathbf{0}) \geq c_0\,|||\boldsymbol{U}|||^2 .$$

□

3 Finite Element Approximation

For the finite element approximation, we assume that the domain Ω is a polygon and that $\mathcal{T}_h$ is a partition of Ω into finite elements $\Omega = \bigcup_{T\in\mathcal{T}_h} T$ with $h = \max\{\mathrm{diam}(T) : T \in \mathcal{T}_h\}$. Assume that the triangulation $\mathcal{T}_h$ is regular and satisfies the inverse assumption [11]. The grid size is defined as $h = \sqrt{2A}/\sqrt{N}$, where A is the area of the domain and N is the number of elements in $\mathcal{T}_h$. Let $P_r(T)$ denote the standard space of degree r polynomials on element T. Define finite element spaces for the approximate of $(\mathbf{u}, p, \boldsymbol{\tau}_s, \boldsymbol{\tau}_p)$:

$$
\begin{aligned}
\boldsymbol{V}^h &= \{\mathbf{v}^h \mid \mathbf{v}^h \in \mathbf{V}\cap(C^0(\Omega))^2,\ \mathbf{v}^h|_T \in P_{r+1}(T)^2\ \forall T\in\mathcal{T}_h\},\\
Q^h &= \{q^h \mid q^h \in Q\cap C^0(\Omega),\ q^h|_T \in P_{r+1}(T)\ \forall T\in\mathcal{T}_h\},\\
\boldsymbol{\Sigma}_s^h &= \{\boldsymbol{\sigma}^h \mid \boldsymbol{\sigma}^h \in \boldsymbol{\Sigma}_s\cap(C^0(\Omega))^{2\times2},\ \boldsymbol{\sigma}^h|_T \in P_{r+1}(T)^{2\times2}\ \forall T\in\mathcal{T}_h\},\\
\boldsymbol{\Sigma}_p^h &= \{\boldsymbol{\sigma}^h \mid \boldsymbol{\sigma}^h \in \boldsymbol{\Sigma}\cap(C^0(\Omega))^{2\times2},\ \boldsymbol{\sigma}^h|_T \in P_{r+1}(T)^{2\times2}\ \forall T\in\mathcal{T}_h\}.
\end{aligned}
$$

Let $\boldsymbol{\Phi}^h := \mathbf{V}^h \times Q^h \times \boldsymbol{\Sigma}_s^h \times \boldsymbol{\Sigma}_p^h$ be finite element subspaces of $\boldsymbol{\Phi}$ with the following approximation properties. Let $S^h = \{u \in C^0(\Omega) : u|_T \in P_{r+1}(T)\ \forall T \in \mathcal{T}_h\}$ admit the property

$$\inf_{u^h\in S^h}\left\|u - u^h\right\|_l \leq Ch^m\|u\|_{m+l}\,\forall u \in H^{m+l}(\Omega), \tag{35}$$

for $l = 0, 1$.

The discrete minimization problem is to choose $\boldsymbol{U}^h \in \boldsymbol{\Phi}^h$ such that

$$J(\boldsymbol{U}^h; \mathbf{F}) = \inf_{\boldsymbol{V}^h \in \boldsymbol{\Phi}^h} J(\boldsymbol{V}^h; \mathbf{F}), \tag{36}$$

where $\boldsymbol{U}^h = (\mathbf{u}^h, p^h, \boldsymbol{\tau}_s^h, \boldsymbol{\tau}_p^h)$ and $\boldsymbol{V}^h = (\mathbf{v}^h, q^h, \boldsymbol{\sigma}_s^h, \boldsymbol{\sigma}_p^h)$. Let the differential operators $L_1(\boldsymbol{U}^h)$, $L_2(\mathbf{u}^h)$, $L_3(\mathbf{u}^h, \boldsymbol{\tau}_s^h)$, and $L_4(\mathbf{u}^h, \boldsymbol{\tau}_p^h)$ be defined so that the finite element approximation to (36) is equivalent to seek $\boldsymbol{U}^h \in \boldsymbol{\Phi}^h$ such that

$$\mathfrak{B}(\boldsymbol{U}^h; \boldsymbol{V}^h) = \mathfrak{F}(\boldsymbol{V}^h) \; \forall \boldsymbol{V}^h \in \boldsymbol{\Phi}^h, \tag{37}$$

where $\boldsymbol{U}^h = (\mathbf{u}^h, p^h, \boldsymbol{\tau}_s^h, \boldsymbol{\tau}_p^h)$, $\boldsymbol{V}^h = (\mathbf{v}^h, q^h, \boldsymbol{\sigma}_s^h, \boldsymbol{\sigma}_p^h)$, and

$$\begin{aligned}
&\mathfrak{B}(\boldsymbol{U}^h; \boldsymbol{V}^h) \\
&= \int_\Omega L_1^T\left(\boldsymbol{U}^h\right) \cdot L_1\left(\boldsymbol{V}^h\right) d\Omega + K \int_\Omega L_2^T(\mathbf{u}^h) L_2(\mathbf{v}^h) d\Omega \\
&\quad + \int_\Omega L_3^T\left(\mathbf{u}^h, \boldsymbol{\tau}_s^h\right) : L_3\left(\mathbf{v}^h, \boldsymbol{\sigma}_s^h\right) d\Omega + W \int_\Omega L_4^T\left(\mathbf{u}^h, \boldsymbol{\tau}_p^h\right) : L_4\left(\mathbf{v}^h, \boldsymbol{\sigma}_p^h\right) d\Omega
\end{aligned} \tag{38}$$

and

$$\mathfrak{F}(\boldsymbol{V}^h) = \int_\Omega \mathbf{f}_1 \cdot L_1\left(\boldsymbol{V}^h\right) + W \int_\Omega \mathbf{f}_2 \cdot L_4\left(\mathbf{v}^h, \boldsymbol{\sigma}_p^h\right) d\Omega.$$

Using Theorem1 and the approximation property (35), the following error estimate is established.

Theorem 2 *Consider approximating the solution to (11)–(15) through the discrete minimization problem (36) under the assumption in (10). Assume that the solution $\boldsymbol{U}$ to (17) is regular enough such that $\boldsymbol{U} \in \boldsymbol{\Phi} \cap (\mathbf{H}^{m+1}(\Omega))^2 \times H^{m+1}(\Omega) \times (\mathbf{H}^{m+1}(\Omega))^{2\times 2} \times (\mathbf{H}^{m+1}(\Omega))^{2\times 2}$ and M is small, then the LS approximation $\boldsymbol{U}^h \in \boldsymbol{\Phi}^h$ satisfies*

$$\left|\left|\left| \boldsymbol{U}^h - \boldsymbol{U} \right|\right|\right| \leq Ch^m \left(\|\boldsymbol{\tau}_s\|_{m+1} + \left\|\boldsymbol{\tau}_p\right\|_{m+1} + \|p\|_{m+1} + Re\, \|\mathbf{u}\|_{m+1} \right), \tag{39}$$

for $m \leq r + 1$.

Proof The orthogonal property $\mathfrak{B}(\boldsymbol{U} - \boldsymbol{U}^h; \boldsymbol{V}^h) = 0$ for all $\boldsymbol{V}^h \in \Phi^h$ and Theorem 1 directly lead to the bound

$$\left|\left|\left| \boldsymbol{U}^h - \boldsymbol{U} \right|\right|\right| \leq \inf_{V^h \in \Phi^h} \frac{c_1}{c_0} \left|\left|\left| \boldsymbol{V}^h - \boldsymbol{U} \right|\right|\right|_1,$$

which yields the desired error bound using the approximation property in (35). □

Note that the use of continuous piecewise linear polynomials for all unknowns yields the following rates:

$$\|\boldsymbol{\tau}_s^h - \boldsymbol{\tau}_s\|_0 = O(h), \; \|\boldsymbol{\tau}_p^h - \boldsymbol{\tau}_p\|_0 = O(h), \; \|p^h - p\|_0 = O(h),$$

and

$$\|\mathbf{u}^h - \mathbf{u}\|_1 = O(h).$$

The theoretically predicted error bounds are only $O(h)$ in the L^2-norm for $\boldsymbol{\tau}_s$, $\boldsymbol{\tau}_p$, and p, $O(h)$ in the H^1-norm for $\mathbf{u}$. Hence, we have the optimal convergence rate of the velocity in

the H^1-norm and suboptimal convergence rates of the stress and pressure in the L^2-norm. For the finite element space used here, the nonlinear functional norm $g^{1/2}$ in (18) is an a posteriori error estimate for the LS method. In Sect. 4 our numerical experiments will show that the a posteriori error bound is consistent with the a priori error bound, i.e., the error bound for $g^{1/2}$ is $O(h)$ when the continuous piecewise linear finite elements are used for the approximations of all variables.

Next, we present a Newton iteration scheme for solving the linear PTT model by using the LS method, as shown in [13]. Denote the unknowns by $\boldsymbol{U} = (\mathbf{u}, p, \boldsymbol{\tau}_s, \boldsymbol{\tau}_p) \in \boldsymbol{\Phi}$ and the steady state residual of (3) by

$$\mathbf{R}(\boldsymbol{U}) := \begin{bmatrix} Re(\mathbf{u}\cdot\nabla\mathbf{u}) - \nabla\cdot\boldsymbol{\tau}_p - \nabla\cdot\boldsymbol{\tau}_s + \nabla p - \mathbf{f} \\ \nabla\cdot\mathbf{u} \\ \boldsymbol{\tau}_s - 2\beta\mathbf{D}(\mathbf{u}) \\ \boldsymbol{\tau}_p + We(\mathbf{u}\cdot\nabla\boldsymbol{\tau}_p - A(\nabla\mathbf{u},\boldsymbol{\tau}_p)) + \frac{\epsilon We}{(1-\beta)} tr(\boldsymbol{\tau}_p)\boldsymbol{\tau}_p - 2(1-\beta)\mathbf{D}(\mathbf{u}) \end{bmatrix}. \quad (40)$$

We now approximate the solution to $\mathbf{B}(\boldsymbol{U}) := \mathbf{P}^{\mathbf{T}}\mathbf{R}(\boldsymbol{U}) = 0$ with a diagonal matrix $\mathbf{P}$ whose diagonal entries consist of LS weighting functions for the momentum, continuity, velocity gradient, and constitutive equations by an inexact Newton iteration. The ℓ^{th} iterate approximated on Ω is given by $\boldsymbol{U}_\ell^h$. Each linear step in this iterative procedure is found by solving for the update $\boldsymbol{S}_\ell^h = \boldsymbol{U}_{\ell+1}^h - \boldsymbol{U}_\ell^h$ in the linear problem

$$\mathbf{J}(\boldsymbol{U}_\ell^h)\boldsymbol{S}_\ell^h = -\mathbf{B}(\boldsymbol{U}_\ell^h), \quad (41)$$

where $\mathbf{J}$ is the Jacobian of $\mathbf{B}$. The new approximation is given by $\boldsymbol{U}_{\ell+1}^h = \boldsymbol{U}_\ell^h + \boldsymbol{S}_\ell^h$. Each linear problem (41) is cast as an LS minimization problem by defining the linear LS functional

$$J_\ell(\boldsymbol{S}_\ell^h) = \|\mathbf{J}(\boldsymbol{U}_\ell^h)\boldsymbol{S}_\ell^h + \mathbf{B}(\boldsymbol{U}_\ell^h)\|^2, \quad (42)$$

and then finding $\boldsymbol{S}_\ell^h \in \boldsymbol{\Phi}^h$ such that

$$J_\ell(\boldsymbol{S}_\ell^h) \le J_\ell(\boldsymbol{V}_\ell^h)\ \forall \boldsymbol{V}_\ell^h \in \boldsymbol{\Phi}^h. \quad (43)$$

4 Numerical Results

The governing equations are solved in two different domains in this section. The first is a square test domain, where exact boundary conditions are imposed on the boundary to measure convergence rates. To further illustrate the capability of the LS scheme, the method is applied to a planar channel problem and a slot channel problem. Linear basis functions are considered for all variables, and the initial $\mathbf{u}_1$ and $\boldsymbol{\tau}_{p1}$ in Sect. 2 are set to zero in all computations.

4.1 Flows in a Planar Channel

We consider a square test domain $[0, 1] \times [0, 1]$ with exact boundary conditions and non-zero right-hand sides determined by the exact solutions to measure convergence rates. Due to the symmetry along $y = 0$, the computed domain is reduced to the half. The velocity $\mathbf{u} = [u\ , v]^T$ is specified on the inflow, outflow, and wall boundaries. Pressure p is fixed at the point where the outflow boundary meets the symmetry boundary. On the symmetry boundary, the y-component of $\mathbf{u}$ and $\boldsymbol{\tau}_{pxy}$ vanish. At the wall boundaries $\mathbf{u} = \mathbf{0}$ is imposed. Because there is no analytical solution for the stress of the PTT model, we impose the inflow stress boundary condition and the source terms determined by the analytical solution of the

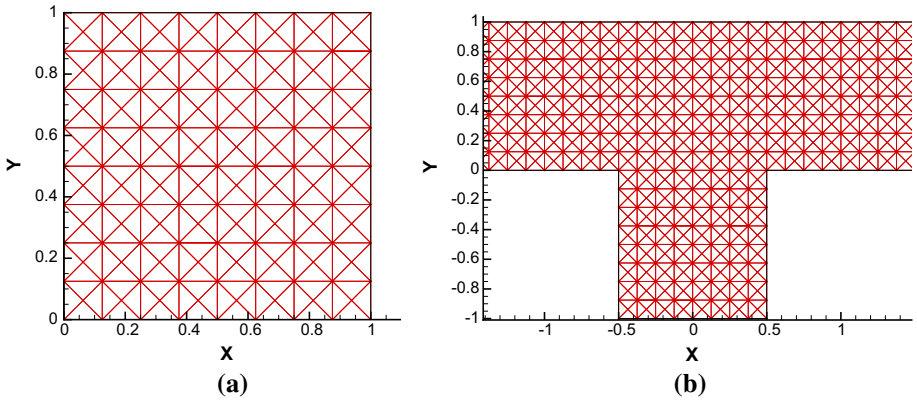

Fig. 2 Uniform Meshes C and T with 8 partitions per unit length. **a** Mesh C. **b** Mesh T

Giesekus model [6]

$$\boldsymbol{\tau}_{pxx} = 2We(1-\beta)\dot{\gamma}^2,\ \boldsymbol{\tau}_{pxy} = (1-\beta)\dot{\gamma},\ \boldsymbol{\tau}_{pyy} = 0, \tag{44}$$

where $\dot{\gamma} = \frac{\partial u}{\partial y}$. Let $\mathbf{u} = [u,\ v]^T = [1-y^4,\ 0]^T$ at the inflow and outlet boundaries. Based on the exact solutions the sources terns of (11) and (14) are given by

$$\mathbf{f}_1 = \begin{bmatrix} 12y^2 - 2x \\ 0 \end{bmatrix}, \tag{45}$$

$$\mathbf{f}_2 = \begin{bmatrix} 1024\epsilon We^3(1-\beta)y^{12} & -128\epsilon We^2(1-\beta)y^9 \\ -128\epsilon We^2(1-\beta)y^9 & 0 \end{bmatrix}, \tag{46}$$

respectively. In the convergence test, the parameters are set as $\beta = 1/9, 1-\beta = 8/9$, $Re = 1$, $We = 0.2$, and $\epsilon = 0.2$. The numerical simulation is performed using first order polynomials for all variables. We discretize the resulting linearized model through the Newton method.

To illustrate the convergence of the method and the effect of mass conservation, we use three uniform criss-cross Meshes C with 16, 32, and 64 partitions per unit length in Fig. 2. Previous studies [6,15] have shown that mass conservation is not favorable in LS formulations when low-order basis functions are used. To appropriately adjust the weight given by $K = 10^m$ in (16), we iterate on m for $3 \le m \le 5$ to compute $g_m^{1/2}$ in (18) as shown in [15]. Figure 3a shows the convergence of $g_m^{1/2}$ with respect to $K = 10^m$, ranging from 10^3 to 10^5, on Mesh C with 16, 32, and 64 partitions per unit length. Figure 3a also presents numbers of Newton steps for all cases. The reduction in $g_m^{1/2}$ for the case of 64 partitions is lower than that for the 8 partitions. The convergence of the iteration scheme for $K = 10^m$ is confirmed when $\delta g_m^{1/2} := |g_{m+1}^{1/2} - g_m^{1/2}|/g_{m+1}^{1/2} < 10^{-4}$, and we observed that this can be achieved with $K = 10^5$. Thus, the mass conservation parameter $K = 10^5$ is chosen in the LS formulation in this example. The errors of LS solutions are presented in Figure 3b, which shows that the resulting convergence rates for the velocity converge to the optimal convergence rate $O(h)$ in the H^1-norm. The figure also shows that convergence rates for the pressure and stresses are suboptimal $O(h)$ in the L^2-norm. We also investigate convergence rates of $g^{1/2}$ for various combinations of modeling parameters We, ϵ and Re. Figure 4 shows convergence rates of $g^{1/2}$ at $(We,\ \epsilon,\ Re/10)$=$(We,\ 0.2,\ 1)$, $(0.2,\ \epsilon,\ 1)$, and $(0.2,\ 0.2,\ Re/10)$, where one of We, ϵ and $Re/10$ ranges from 0.1 to 1 while the

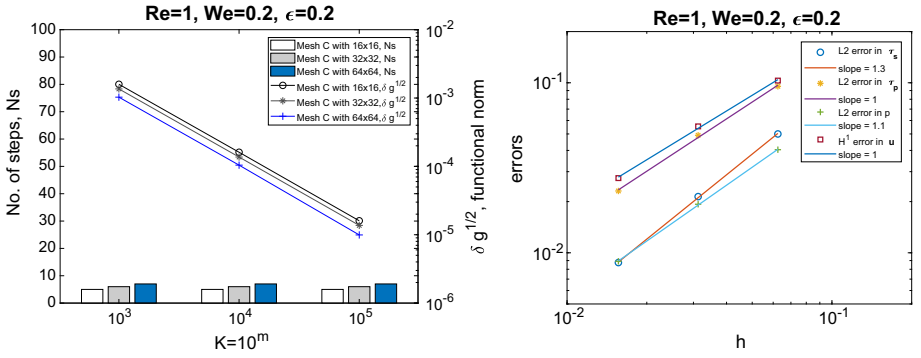

Fig. 3 The LS solutions using $K = 10^5$ on Mesh C with 16, 32, and 64 partitions per unit length at $Re = 1$, $We = 0.2$, and $\epsilon = 0.2$. **a** Reduction of functional norm $\delta g_m^{1/2}$ on Mesh C with 16 (o), 32 (*), and 64 (+) in nonlinear nested iteration for various weights $K = 10^m$, m ranging from 3 to 5. Here no. of steps Ns means the number of iterative steps for convergence. **b** L^2 errors in $\boldsymbol{\tau}_s$ (o), $\boldsymbol{\tau}_p$ (*), and p (+), and H^1 errors in **u** (□) of LS solutions using $K = 10^5$

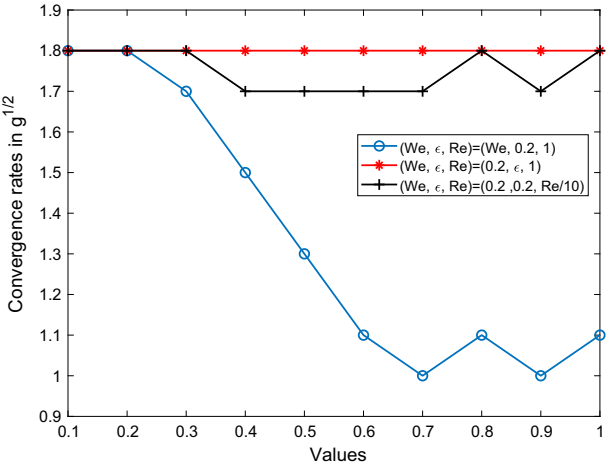

Fig. 4 The convergence rates of the LS solutions in $g^{1/2}$ at $(We,\ \epsilon,\ Re/10)$=$(We,\ 0.2,\ 1)$, $(0.2,\ \epsilon,\ 1)$, and $(0.2,\ 0.2,\ Re/10)$ for various We, ϵ, and $Re/10$ values ranging from 0.1 to 1

other two are fixed. Note that the convergence rates are much higher than the expected rate ($g_m^{1/2} \approx J^{1/2} = O(h)$) for $We < 0.5$, but the rates are close to $O(h)$ for $0.5 \leq We \leq 1$. This is consistent with the theoretical predication in Sect. 3 without the small We condition. Moreover, the convergence rate of $g_m^{1/2}$ with respect to ϵ or Re is much higher than the expected rate $O(h)$ and close to 1.8. Results show that We effects on the solutions are higher than ϵ and Re. However, the numerical results indicate that the LS error estimator $g^{1/2}$ shows at least the first-order convergence rate when the equal-order linear polynomial is used for all variables.

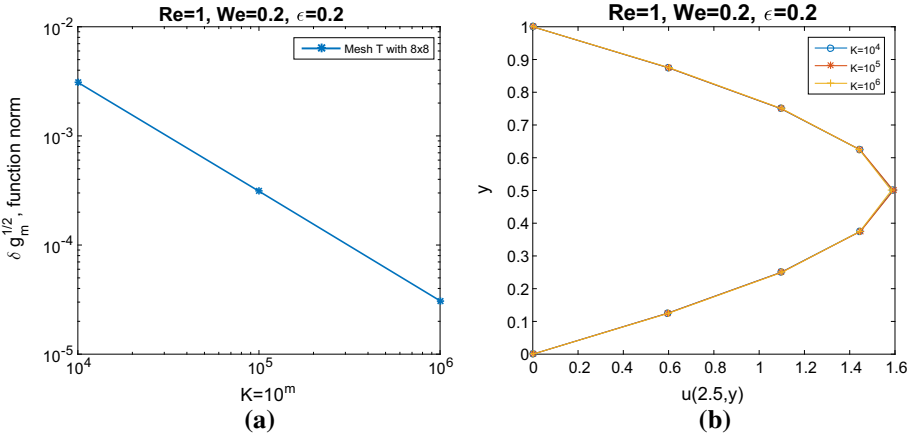

Fig. 5 **a** Reduction of $\delta g_m^{1/2}$ $(*)$ functional norm of LS solutions for $Re = 1$, $\epsilon = 0.2$, and $We = 0.2$ on Mesh T using $K = 10^m$ with $m = 4$ to 6. **b** Profiles of the horizontal velocity u(2.5,y) of the LS method with $K = 10^m$ with $m = 4$ to 6 using Mesh T

4.2 Flows Past a Transverse Slot

To further demonstrate the capability of the numerical algorithm in the PTT model, we apply the LS method to analyze the flow through a slot channel (Fig. 1). Here, x (the flow direction) is in the range of $-2.5 \leq x \leq 2.5$ and a contraction occurs at $x = 0$. The length (l) and width (d) of the slot are both 1 unit; therefore, the width (h) of the channel is also 1 unit. The boundary conditions include those at the inlet, outlet, and wall boundaries. Let $\mathbf{u} = (u, v)$ and $\boldsymbol{\tau_p}$ be specified at inflow boundaries as

$$u = 6(y - y^2), \ v = 0, \tag{47}$$

$$\boldsymbol{\tau}_{pxx} = 2We(1-\beta)\dot{\gamma}^2, \ \boldsymbol{\tau}_{pxy} = (1-\beta)\dot{\gamma}, \ \boldsymbol{\tau}_{pyy} = 0, \tag{48}$$

$\dot{\gamma} = \frac{\partial u}{\partial y}$ and $\mathbf{u} = \mathbf{0}$ at the wall boundaries. The pressure $p = 0$ and the velocity $v = 0$ are specified at the outflow boundary. These boundary conditions are also used in [14,21]. The analytical prediction of hole pressure may be obtained by substituting $N_1 = \boldsymbol{\tau}_{pxx} - \boldsymbol{\tau}_{pyy} = 2We(1-\beta)\dot{\gamma}^2$ and $\boldsymbol{\tau}_{pxy} = (1-\beta)\dot{\gamma}$ into (9), and then carrying out the integral by changing the variable from $\boldsymbol{\tau} = \boldsymbol{\tau}_{pxy}$ to $\dot{\gamma}$:

$$P_h = \int_0^{\tau_w^b} \frac{N_1}{2\boldsymbol{\tau}} d\boldsymbol{\tau} = \int_0^{\dot{\gamma}_w^b} We(1-\beta)\dot{\gamma} d\dot{\gamma} = \frac{1}{2}We(1-\beta)(\dot{\gamma}_w^b)^2 = \frac{1}{4}N_{1,w}^b. \tag{49}$$

In (11)−(15), the parameters ($Re, \beta, 1-\beta, \epsilon, We$) are required to describe the fluid rheology. In our test, the parameters are set as $Re = 1$, $\beta = 1/9$, and $1 - \beta = 8/9$. To illustrate the convergence of the LS method, we use the uniform criss-cross Mesh T shown in Fig. 2b for the linear PTT model at $We = 0.2$ and $\epsilon = 0.2$.

First, the optimal weight function $K = 10^m$ is chosen in the similar manner to the first example; we iterate on m for $4 \leq m \leq 6$ for the functional $g_m^{1/2}$ in (18). As shown in Fig. 5a $\delta g_m^{1/2} = |g_{m+1}^{1/2} - g_m^{1/2}|/g_{m+1}^{1/2}$ is less than 10^{-4} at $m = 6$, therefore, $K = 10^6$ is chosen as an optimal weight for the LS formulation. Figure 5b shows velocity profiles at the outlet ($x = 2.5$), indicating that the velocity profiles are identical for $K \geq 10^4$. To illustrate the convergence of the LS method, streamlines obtained using uniform meshes T, T1, and T2

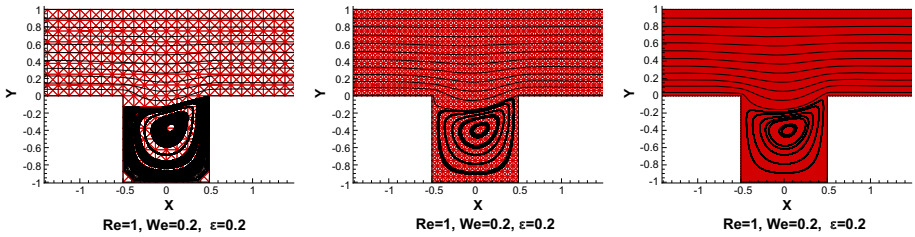

(a) Mesh T **(b)** Mesh T1 **(c)** Mesh T2

Fig. 6 Streamlines for flow over a slot ($d/h = 1, l/h = 1$) using the LS method on uniform Meshes **a** T with 1536 elements, **b** T1 with 6144 elements, and **c** T2 with 24576 elements at $Re = 1$, $We = 0.2$, and $\epsilon = 0.2$

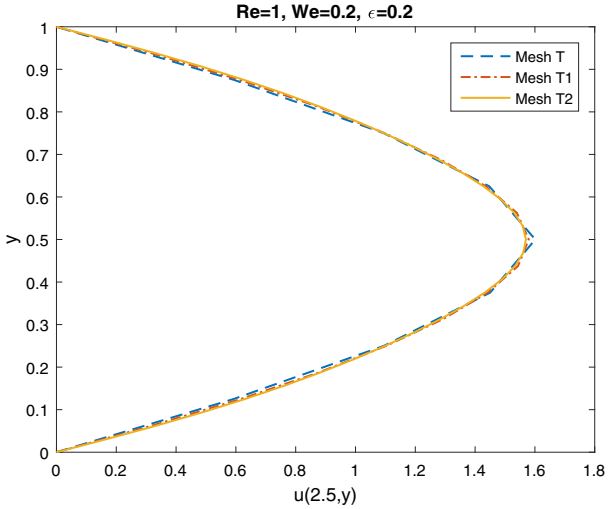

Fig. 7 Plots of $u(2.5, y)$ along the line $0 \le y \le 1$ on uniform Meshes T, T1, and T2 at $Re = 1$, $We = 0.2$, and $\epsilon = 0.2$

with 8, 16, and 32 partitions per unit length are plotted in Fig. 6; the figure shows convergent streamlines of the LS method for the linear PTT model. Figure 7 shows profiles of $u(2.5, y)$ for $0 \le y \le 1$ obtained using Meshes T, T1, and T2 with numbers of elements $N_0 = 1536$, $N_1 = 6144$, and $N_2 = 24576$, respectively.

In Fig. 8, we present the reduction of the functional norm $\Delta g^{1/2}_{(k)}/\Delta N_k = |g^{1/2}_{(k)} - g^{1/2}_{(k-1)}|/|N_k - N_{k-1}|$ versus the number of elements N_k for k =1, 2, where $g^{1/2}_{(k)}$ denotes the functional value by Mesh Tk. We consider modeling parameters $(We,\ \epsilon) = (We, 0.2)$ and $(We, 0.5)$ for $0.1 \le We \le 0.5$ and $We = 1$. An uniform mesh convergence for N_k is confirmed when $\Delta g^{1/2}_{(k)}/\Delta N_k < 10^{-4}$, which can be achieved with $k = 2$ at $(We, 0.2)$ for $We \le 0.3$ in Fig. 8a and $(We, 0.5)$ for $We \le 1$ in Fig. 8b. The results show that We effects on the solutions at a low ϵ are higher than that at a high ϵ. We performed extensive numerical tests for grid convergence at various $(We,\ \epsilon)$. The LS method and flow characteristics are well illustrated by the LS solutions presented in Fig. 9 for $(We,\ \epsilon)$= (0.2, 0.2), (0.2, 0.5), and (1, 0.5) on Mesh T2.

We study the effects of the weight W on LS solutions in (16). Figure 9 illustrates the reduction in the nonlinear functional norm on LS solutions without and with W using Meshes

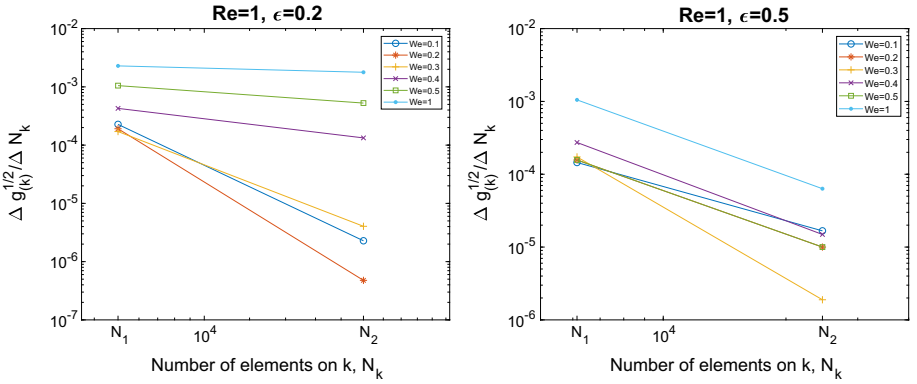

Fig. 8 Reduction of functional norm $\Delta g_{(k)}^{1/2}/\Delta N_k$ versus the number of elements N_k at $k = 1,\ 2$ for the LS method using Mesh Tk at $Re = 1$, with **a** (We, ϵ)=$(We, 0.2)$ and **b** (We, ϵ)=$(We, 0.5)$ for $We = 0.1$ (o), 0.2 $(*)$, 0.3 $(+)$, 0.4 $(\times)$, 0.5 $(\square)$, and 1 $(\bullet)$

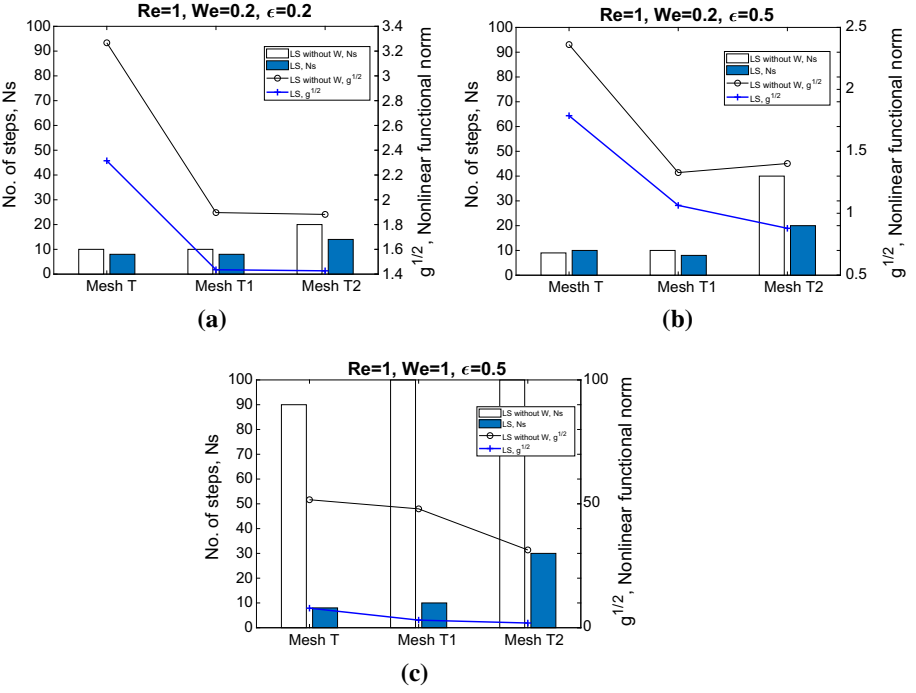

Fig. 9 Reduction of nonlinear $g^{1/2}$ functional norm using Meshes T, T1, and T2 for the LS without $W(o)$ and the LS $(+)$ for $Re = 1$, with **a** $We = 0.2$ and $\epsilon = 0.2$, **b** $We = 0.2$ and $\epsilon = 0.5$, and **c** $We = 1$ and $\epsilon = 0.5$. Here no. of steps Ns means the number of iterative steps for convergence

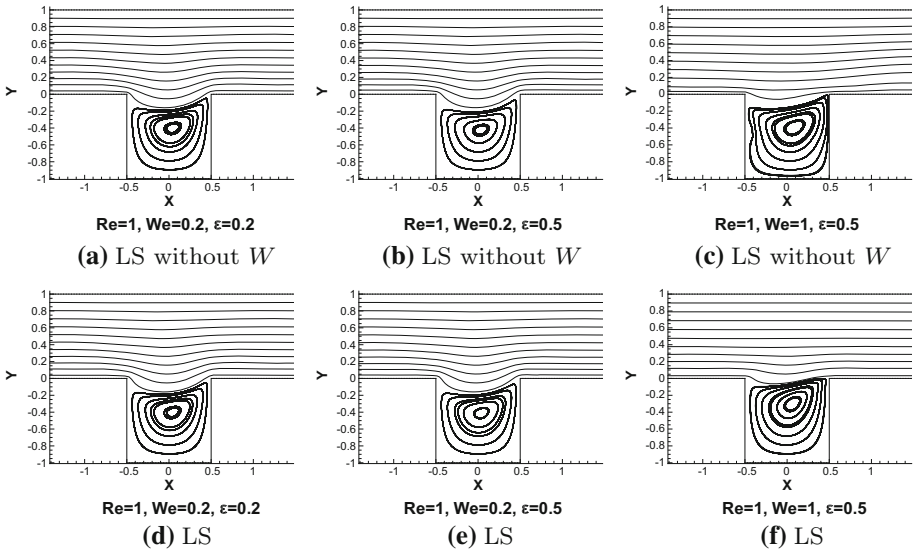

(a) LS without W **(b)** LS without W **(c)** LS without W

(d) LS **(e)** LS **(f)** LS

Fig. 10 Streamlines for flow over a slot ($d/h = 1, l/h = 1$) using the LS method on uniform Mesh T2 for LS without W with **a** $We = 0.2$ and $\epsilon = 0.2$, **b** $We = 0.2$ and $\epsilon = 0.5$, **c** $We = 1$ and $\epsilon = 0.5$, and for LS with **d** $We = 0.2$ and $\epsilon = 0.2$, **e** $We = 0.2$ and $\epsilon = 0.5$, **f** $We = 1$ and $\epsilon = 0.5$

T, T1, and T2 for $We = 0.2$ and $\epsilon = 0.2$ (Fig. 9a), $We = 0.2$ and $\epsilon = 0.5$ (Fig. 9b), and $We = 1$ and $\epsilon = 0.5$ (Fig. 9c). We observe that the reduction in $g^{1/2}$ for the LS solution with W is higher than that for the LS solution without W for all cases. As shown in Fig. 9, the iterative process exceeds the maximum number of Newton steps (100) for two cases of LS without W using Meshes T1 and T2 at $We = 1$ and $\epsilon = 0.5$. Therefore, the number of iterative steps can be reduced by our LS method in almost all cases, i.e., the LS solution with W is more effective than that without W. Figure 10 shows streamlines of the LS solution without W and the LS solution with W for $We = 0.2$ and $\epsilon = 0.2$, $We = 0.2$ and $\epsilon = 0.5$, and $We = 1$ and $\epsilon = 0.5$. We obtain the smooth streamlines of the LS solutions with W for all cases. The results reveal that streamlines of the LS solution without W (Fig. 10a and b) and the LS solution with W (Fig. 10d and e) are in the agreement, however, those of LS without W near the left side wall are insufficiently smooth for $We = 1$ (Fig. 10c and f). Therefore, the LS solutions can be improved by the weight W for a high We fluid. This is consistent with the results of the a posteriori error estimator $g^{1/2}$ (Fig. 10).

In the next experiment we double the length of the slot and compare numerical results for $l/h = 1$ and $l/h = 2$ with $h = 1$ and $d = 1$ fixed. Figure 11 shows streamlines of the LS solutions for $Re = 1, \epsilon = 0.5$ with $We = 0.1$, 0.5, and 1, respectively. The different vortex development processes are detailed in Fig. 11. The vortex size increases as We increases, and the vortex moves toward the reentrant corners. The size also increases as the depth ratio (l/h) increases, and the vortex occurs at the bottom of the slot when $l/h = 2$. These results are consistent with those obtained in [10,21]. Figure 12 shows the profiles of the horizontal velocity u along the vertical centreline for various We numbers ($We = 0.1$, 0.5, and 1) when $l/h = 1$ (Fig. 12a) and $l/h = 2$ (Fig. 12b). The plots indicate that when We increases, its effects become more dominant and the profiles at the line $y = 0.5$ resemble shapes sharper than a parabola ($We = 0.1$). Figure 13 shows two profiles of the hole pressure P_h and the wall normal-stress difference $N^b_{1,w}$ for various We numbers ($(0 \leq We \leq 1)$) at $Re = 1$ and

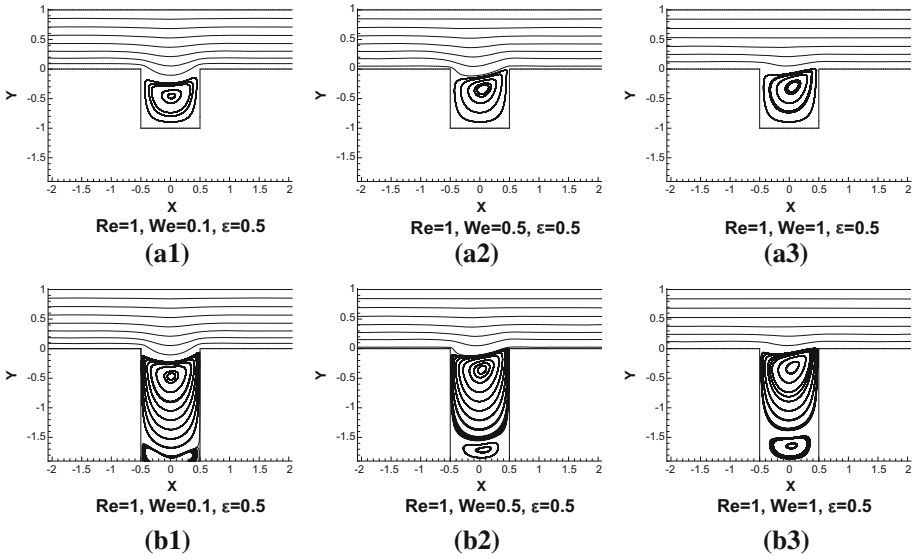

Fig. 11 Streamlines for flow over a slot ($d/h = 1$) in the LS solutions at $Re = 1$ and $\epsilon = 0.5$ for $l/h = 1$ with **a1** $We = 0.1$, **a2** $We = 0.5$, and **a3** $We = 1$ and for $l/h = 2$ with **b1** $We = 0.1$, **b2** $We = 0.5$, and **b3** $We = 1$

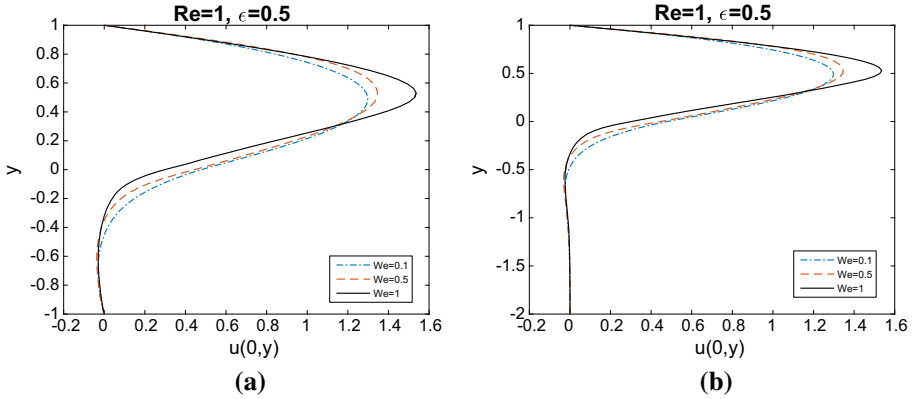

Fig. 12 Plots of $u(0, y)$ along the centreline using the LS method at $Re = 1$, $\epsilon = 0.5$, $We = 0.1$, $We = 0.5$, and $We = 1$ for **a** $-1 \leq y \leq 1$ ($l/h = 1$) and **b** $-2 \leq y \leq 1$ ($l/h = 2$)

$\epsilon = 0.5$. For the low We fluid ($0 \leq We \leq 0.3$), an increase in We causes an increase in the values of P_h and $N^b_{1,w}$. For $0.3 < We \leq 1$, a decrease in We causes a decrease in the values of P_h and $N^b_{1,w}$. The plots of P_h agree with $N^b_{1,w}/4$ for the low We fluids. Figure 13 indicates that the analytical prediction in (49) and the numerical results are close. The results are consistent with those obtained in [20] for the low We fluids. In addition, the results show that the two values of P_h and $N^b_{1,w}/4$ grow apart as We increase.

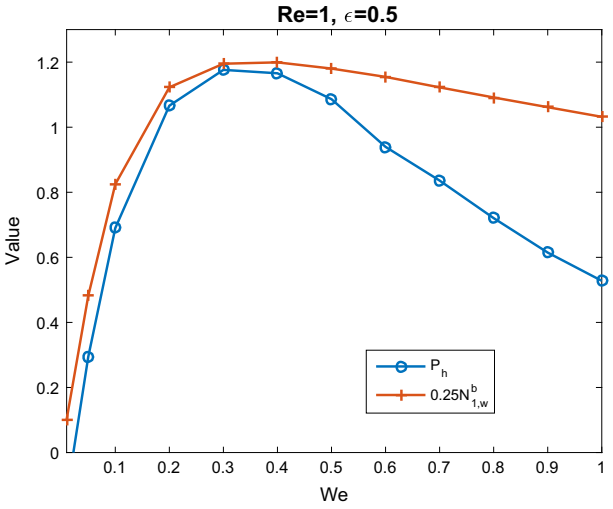

Fig. 13 The results in P_h and $N^b_{1,w}/4$ versus We numbers for the linear PTT model at $Re = 1$ and $\epsilon = 0.5$ past a slot in the channel ($d/h = 1, l/h = 1$)

5 Conclusion

We considered an LS method to simulate linear PTT viscoelastic fluid flows. The model problems considered are flows in a planar channel and a transverse slot, respectively. The linearized viscoelastic problem by the Newton's method was solved through the minimization of a LS functional with two weight functions. The weight functions were used to prevent loss of mass conservation and convergence at high Weissenberg numbers, when low order basis functions are used. We provided a detailed analysis of an a priori error estimate for the linearized viscoelastic system and presented numerical results to support the estimate. Using continuous piecewise linear finite element spaces for all variables and appropriately weighted continuity and constitutive equations, respectively, we obtained the first order convergence rate in the H^1-norm for velocity, in the L^2-norm for the viscous and polymer stresses, and pressure, respectively; these results agree with the theoretically predicted estimate. We also discussed the physical parameter effects of the LS method for the slot channel problem. The resulting hole pressure was evaluated numerically for various We numbers, and compared with that derived from the HP theory. The results show that the HP equation is valid for viscoelastic fluid flows with a low We and that streamlines of the flow agree with published results.

Acknowledgements The first author gratefully acknowledges the financial support provided in part by the Ministry of Science and Technology of Taiwan under Grant 107-2115-M-160-001-MY2. The second author is grateful for the financial support provided in part by the US National Science Foundation under Grant DMS-1418960.

References

1. Alves, M.A., Oliveira, P.J., Pinho, F.T.: Benchmark solutions for the flow of Oldroyd-B and PTT fluids in planar contractions. J. Non-Newton. Fluid Mech. **110**, 45–75 (2003)

2. Azaiez, J., Guénette, R., Ait-Kadi, A.: Numerical simulation of viscoelastic flows through a planar contraction. J. Non-Newton. Fluid Mech. **62**, 253–277 (1996)
3. Bochev, P.B., Gunzburger, M.D.: Finite element methods of least-squares type. SIAM Rev. **40**, 789–837 (1998)
4. Cai, Z., Westphal, C.R.: An adaptive mixed least-squares finite element method for viscoelastic fluids of Oldroyd type. J. Non-Newton. Fluid Mech. **159**, 72–80 (2009)
5. Cai, Z., Manteufeel, T.A., Mccormick, S.F.: First-order system least-squares for velocity–vorticity–pressure form of the Stokes equations, with application to linear elastically. Electron. Trans. Numer. Anal. **3**, 150–159 (1995)
6. Chen, T.F., Cox, C.L., Lee, H.C., Tung, K.L.: Least-squares finite element methods for generalized Newtonian and viscoelastic flows. Appl. Numer. Math. **60**, 1024–1040 (2010)
7. Chen, T.F., Lee, H., Liu, C.C.: Numerical approximation of the Oldroyd-B model by the weighted least-squares/discontinuous Galerkin method. Numer. Methods Partial Diff. Equ. **29**, 531–548 (2013)
8. Coronado, O.M., Arora, D., Behr, M., Pasquali, M.: Four-field Galerkin/least-squares formulation for viscoelastic fluids. J. Non-Newton. Fluid Mech. **140**, 132–144 (2006)
9. Higashitani, K., Pritchard, W.G.: A kinematic calculation of intrinsic errors in pressure measurements made with holes. Trans. Soc Rheol. **16**, 688–696 (1972)
10. Huilgol, R.R., Phan-Thien, N.: Fluid Mechanics of Viscoelasticity: General Principles, Constitutive Modelling, Analytical and Numerical Techniques. Elsever, Amsterdam (1997)
11. Lee, H.C.: A nonlinear weighted least-squares finite element method for the Oldroyd-B viscoelastic flow. Appl. Math. Comput. **219**, 421–434 (2012)
12. Lee, H.C.: An adaptively refined least-squares finite element method for generalized Newtonian fluid flows using the Carreau model. SIAM J. Sci. Comput. **36**, 193–218 (2014)
13. Lee, H.C.: A nonlinear weighted least-squares finite element method for the Carreau–Yasuda non-Newtonian model. J. Math. Anal. Appl. **432**, 844–861 (2015)
14. Lee, H.C.: Numerical simulations of viscoelastic fluid flows using a least-squares finite element method based on von Mises stress criteria. Int. J. Appl. Phys. Math. **7**, 157–164 (2017)
15. Lee, H.C.: Adaptive weights for mass conservation in a least-squares finite element method. Int. J. Comput. Math. **95**, 20–35 (2018)
16. Liu, J.L.: Exact a posteriori error analysis of the least-squares finite element method. Appl. Math. Comput. **116**, 297–305 (2000)
17. Renardy, M., Hrusa, W.J., Nohel, A.: Mathematical Problems in Viscoelasticity. Wiley, New York (1987)
18. Tanner, R.I., Pipkin, A.C.: Intrinsic errors in hole-pressure measurements. Trans. Soc. Rheol. **13**, 471–484 (1969)
19. Thien, N.P., Tanner, R.I.: A new constitutive equation derived from network theory. J. Math. Anal. Appl **2**, 353–365 (1977)
20. Wu, G.H., Lin, Y.M.: Creeping flow of a polymeric liquid passing over a transverse slot with viscous dissipation. Int. J. Heat Mass Transf. **45**, 4703–4711 (2002)
21. Yin, H.J., Zhong, H.Y., Fu, C.Q., Lei, W.: Numerical simulations of viscoelastic flows through one slot channel. J. Hydrodyn. **19**, 201–216 (2007)
22. Zhou, S., Hou, L.: A weighted least-squares finite element method for Phan-Thien–Tanner viscoelastic fluid. J. Math. Anal. Appl. **436**, 66–78 (2016)